Energy Technology

Generation, Conversion, Storage, Distribution

Accepted Article

Title: The Synergetic Benefits of Passivation Layer and Catalytic Layer on Hematite for Efficient Water Splitting

Authors: Xiaoqin Cheng, Shiyao Cao, Yahuan Huan, Zhiming Bai, Minghua Li, Hailin Wu, Ruxiao Zhang, Wencai Peng, Zhen Ji, and Xiaoqin Yan

The Synergetic Benefits of Passivation Layer and Catalytic Layer on Hematite for Efficient Water Splitting

Xiaoqin Cheng,[a] Shiyao Cao,[a] Yahuan Huan,[a] Zhiming Bai,[b]* Minghua Li,[a] Hailin Wu,[a] Ruxiao Zhang,[a]

Wencai Peng,[a] Zhen Ji,[a] Xiaoqin Yan,[a]*

X. Cheng, S. Cao, Y. Huan, M. Li, P. Wu, H. Wu, R. Zhang, W. Peng, Z. Ji, Prof. X. Yan

State Key Laboratory for Advanced Metals and Materials, School of Materials Science and

Engineering, University of Science and Technology Beijing, Beijing 100083, China

E-mail: xqyan@mater.ustb.edu.cn

Z. Bai

School of Civil and Resource Engineering, University of Science and Technology Beijing, Beijing

100083, China

E-mail: baizhiming2008@126.com

Abstract

In photoelectrochemical （PEC） water splitting systems, overlayer on the surface of semiconductor has always been pursued with tremendous interest. Herein the multicomponent $Fe_2O_3/Fe_xSn_{1-x}O_4/FeOOH$ photoanode is designed to achieve efficient water splitting. The photocurrent density of $Fe_2O_3/Fe_xSn_{1-x}O_4/FeOOH$ photoanode is 1.70 mA cm^{-2} at 1.23 V *vs*. RHE, improved by 121.1%, compared with that of the pristine hematite photoanode (0.77 mA cm^{-2} at 1.23 V *vs*. RHE) under AM 1.5 illumination (100 mW cm^{-2}). Detailed characterization was carried out to explore main factors of photocurrent enhancement. The excellent PEC performance could be attributed to the synergetic benefits of $Fe_xSn_{1-x}O_4$ passivation layer and FeOOH catalyst, which reduce the rate of electron-hole recombination and improve water oxidation reaction kinetics. The results prove a new sight to achieve efficient PEC water splitting.

1. Introduction

In order to solve global environmental problems and accelerate energy transformation, solar energy utilization has attracted wide attention. In a wide variety of solar conversion options, PEC water splitting process is considered one of the most promising choice.[1] This is mostly because, it directly converts the inexhaustible solar energy to chemical energy (H_2 and O_2) and H_2 is regarded as a clean and environmentally benign fuel with water as the only side product. Hematite (α-Fe_2O_3) is an ideal material as photoanode for this application because of its appropriate optical band gap (Eg=2.1 eV),[2] excellent chemical stability in aqueous environments and rich reserves.[3] However, its solar-to-hydrogen (STH) efficiency is lower than the theoretical value, 12.9%.[4] The poor conductivity, short lifetime of photo-generated charge carriers (<10 ps), short hole diffusion length (2–4 nm) and slow

2

oxygen evolution kinetic rate directly cause the low performance of hematite photoanode.[4a]

Various strategies (for example, nanostructured,[5] doped,[6] and surface/interface modified[7]) have

been adopted to improve the performance of hematite photoanode. Thereinto, overlayer on the surface

of the semiconductor is a general strategy to promote charge separation at the surface.[8] Florian *et al.*

used an ultra-thin coating of Al_2O_3 passivation layer (~ 2 nm diameter) on hematite photoanodes by

atomic layer deposition (ALD), resulting in an increased photocurrent density (from 0.24 mA cm^{-2} to

0.85 mA cm^{-2}) at 1.0 V *vs*. RHE.[9] Klahr *et al.* reported that Co−Pi catalytic layer was successfully

coated on hematite photoanodes, and found that the increased water oxidation performance is

attributed to a combination of superior charge separation and increased surface area of the porous

catalytic film.[10] Yu *et al.* observed an obvious cathodic shift in the photocurrent onset potential and a

four-times increase of photocurrent density, which can be attributed to the high reaction area and high

electrocatalytic activity of nanostructured FeOOH.[11]

Therefore, passivation layer can effectively passivate surface defects and suppress the tunneling of

electrons from the hematite to electrolyte. Meanwhile, catalytic layer can greatly promote facile hole

transfer across the interface to decrease charge recombination and improve water oxidation. However,

few studies have investigated the synergistic effects of them. In this paper, the multicomponent

$Fe_2O_3/Fe_xSn_{1-x}O_4/FeOOH$ photoanode was designed, allowing us to investigate if the performance of

PEC water splitting by the photoanode was synergistically enhanced. The results showed that its

current density was obviously improved compared with that of $Fe_2O_3/Fe_xSn_{1-x}O_4$ and $Fe_2O_3/$ FeOOH

photoanodes. The cross-sectional schematic of the $Fe_2O_3/Fe_xSn_{1-x}O_4/FeOOH$ photoanode for water

oxidation is shown in **Figure 1**.

3

2.   **Results and discussion**

The morphology of the pristine hematite was characterized by FESEM as shown in **Figure 2a** and

exhibited an identical surface morphology of wormlike particles, which are 50–100 nm in width. It

can be seen from the cross-section SEM image (inset of **Figure 2a**) that the thickness of hematite film

is about 150 nm. After treatment with $Sn_{(IV)}$ aqueous solution, a thin layer of $Fe_xSn_{1-x}O_4$ formed on the

surface.[4a, 12] (The experimental detail is in the experimental part.) However, there is no obvious

morphological difference. It's the same for FeOOH layer. In the XRD spectrum, they present the same

X-ray diffraction patterns as hematite (α-Fe_2O_3), with a dominant (110) peak at 2q=35.8 indicating

preferential orientation of hematite crystals in the [110] direction.[13] After overlying $Fe_xSn_{1-x}O_4$ layers,

the XRD spectrum has no obvious peak shift or broadening and no additional peaks appeared (see

Figure 2d). The absence of any indication for Sn doping or additional peaks in the XRD spectrum

implies that the modifications due to Sn treatment were limited to the surface of the hematite.[4a]

Similarly, no typical diffraction peaks of FeOOH on the pattern of Fe_2O_3/$Fe_xSn_{1-x}O_4$/FeOOH thin film.

The subsequent TEM results can indicate that the absence of difference in three samples is mainly

caused by the amorphous state and low content of the $Fe_xSn_{1-x}O_4$ layer and FeOOH overlayer.[7b]

The HRTEM image in **Figure 3a** shows clear lattice fringes corresponding to (012) planes of the α-

Fe_2O_3 and a thin amorphous layer wrapping the α-Fe_2O_3 nanoparticle, about 2-3 nm in thickness.

Images derived from Scanning TEM (STEM) and elemental mapping of Fe_2O_3/$Fe_xSn_{1-x}O_4$/FeOOH

thin film show a good distribution of Sn on the surface (see **Figure 3d, 3e**). It is clearly observed that

Sn concentration in the shell is higher than that in the core. This is a powerful evidence of the formation

of $Fe_xSn_{1-x}O_4$ on the hematite. The HRTEM images (see **Figure 3f, 3g**) show that hematite is coated

by a conformal FeOOH nanosheets layer, about 15 nm thick. Actually, there is the $Fe_xSn_{1-x}O_4$ layer between hematite and FeOOH layer, which is covered by FeOOH nanosheets. It can be found that a number of small crystalline domains embedded in an amorphous matrix.[14] The lattice fringe of 2.4 Å corresponds to the reflection from the (111) plane of goethite (α-FeOOH). The result corroborates that outer nanosheets are FeOOH.

In order to determine the chemical composition of bare Fe_2O_3, $Fe_2O_3/Fe_xSn_{1-x}O_4$ and $Fe_2O_3/Fe_xSn_{1-x}O_4/FeOOH$ samples, XPS characterization is performed (**Figure 4**). **Figure 4a** shows the spectra of bare Fe_2O_3, $Fe_2O_3/Fe_xSn_{1-x}O_4$ and $Fe_2O_3/Fe_xSn_{1-x}O_4/FeOOH$ samples. It can be seen that the $Sn_{(IV)}$ is detected in all three samples. The Sn detected in the pristine hematite is from the FTO substrate. The intensity decrease of Sn 3d peaks (centered at 486.5 eV and 494.9 eV) in $Fe_2O_3/Fe_xSn_{1-x}O_4/FeOOH$ samples, compared with $Fe_2O_3/Fe_xSn_{1-x}O_4$, is due to the shallow detection depth of XPS and the 10 nm FeOOH layer. The high resolution XPS spectrum of 2p Fe is shown in **Figure 4b**. Two main peaks at nearly 711 eV and 724 eV are observed, along with two satellite peaks, confirming the presence of only Fe^{3+}.[15] After overlying the $Fe_xSn_{1-x}O_4$ layer, an additional peak at 715.8 eV becomes evident. This peak belongs to the $Sn3p_{3/2}$ spin-orbit split.[4a] **Figure 4c** shows the Sn 3d peaks, and we can find that the Sn $3d_{5/2}$ peaks of $Fe_2O_3/Fe_xSn_{1-x}O_4/FeOOH$ shifted to a lower binding energy than that of $Fe_2O_3/Fe_xSn_{1-x}O_4$. The peak shift may be caused by FeOOH overlayer, which affects the electronic cloud distribution of Sn. The electronegativity of Sn (1.96) is slightly larger than that of Fe (1.83) and far less than that of O (3.44), which finally leads to a lower binding energy.[16] It also proves the good interface contact between $Fe_xSn_{1-x}O_4$ layer and FeOOH layer.

The O 1s spectra of bare Fe_2O_3, $Fe_2O_3/Fe_xSn_{1-x}O_4$ and $Fe_2O_3/Fe_xSn_{1-x}O_4/FeOOH$ samples are shown in **Figure 4(d)-(f)** and the core level peaks are further deconvoluted. It is observed that three types of common peaks, labelled OI, OII and OIII, are found in the three samples. The first peak, OI, represents the lattice oxygen associated with metal oxide (M-O), and the peak OIII, describes the surface adsorbed water molecules and this peak (OIII) also represents the hydrogen-bonded oxygen atom of the linked Fe-O-H.[14, 17] The peak (OIII) of $Fe_2O_3/Fe_xSn_{1-x}O_4/FeOOH$ sample has a higher intensity (for which the (OIII) peak makes up about 35.6% of the total O 1s peak area) than that of the bare Fe_2O_3 and $Fe_2O_3/Fe_xSn_{1-x}O_4$ photoanode (about 23.2% and 23.6%). The exceed part is attributed from the FeOOH coated on hematite.[18] The results identify that the thin layer is FeOOH. The peak (OII), centered at 530.7 eV, corresponds to the $O–Sn^{4+}$ bond.[19] The analyses clearly demonstrate that hematite is coated by $Fe_xSn_{1-x}O_4$ passivation layer. FeOOH layer.

In order to further show the synergetic benefits of the $Fe_xSn_{1-x}O_4$ layer and the FeOOH layer on the photocurrent densities, the following electrochemical tests focus on four different photoanodes (bare Fe_2O_3, $Fe_2O_3/Fe_xSn_{1-x}O_4$, $Fe_2O_3/FeOOH$ and $Fe_2O_3/Fe_xSn_{1-x}O_4/FeOOH$ photoanodes). **Figure 6a** shows photocurrent density -potential (*J-V*) curves of the four different photoanodes under dark and illumination. The photocurrent density of the bare Fe_2O_3 photoanode is 0.77 mA cm^{-2} at 1.23 V *vs*. RHE. Both a high density of surface defect states and slow water oxidation kinetics lead to serious charge recombination at the surface and low photocurrent density. (**Fig. 5a**) When the $Fe_xSn_{1-x}O_4$ passivation layer is added on Fe_2O_3, the water oxidation photocurrent density increases by a factor of about two (0.77 → 1.42 mA cm^{-2} at 1.23 V *vs*. RHE). This is probably due to that the $Fe_xSn_{1-x}O_4$ layer effectively passivates the surface defects and suppresses the tunneling of electrons from the hematite to electrolyte. (**Fig. 5b**) After the FeOOH catalytic layer is deposited on Fe_2O_3, the current onset

6

potential shifts in the cathodic direction by 0.12 V (0.91 → 0.79 V_{RHE}) and the photocurrent density

of Fe_2O_3/FeOOH photoanode increases by 66.2% compared with bare Fe_2O_3 photoanode. The changes

indicate that FeOOH, as an efficient catalyst, promotes facile hole transfer across the interface to

decrease charge recombination and improve water oxidation. (**Fig. 5c**) It can be found that the

Fe_2O_3/$Fe_xSn_{1-x}O_4$/FeOOH photoanode reached the highest current density of 1.70 mA cm^{-2} at 1.23 V

vs. RHE, despite the onset potential slightly right shifted in contrast with that of Fe_2O_3/FeOOH

photoanode. As showed in **Figure 5d**, the highest current density is achieved by the synergetic benefits

of passivation layer and catalytic layer for efficient water splitting. The transient photocurrents are

recorded at a fixed potential of 1.23 V (*vs*. RHE) with light on/off cycles (**Figure 6b**). All the samples

have been tested under illumination for 1 h to investigate the stability of the photoanodes (see **Figure**

6c). **Figure 6d**, **6e** show a serious of photocurrent density-potential (*J-V*) curves with different

preparation parameters. The optimum $Sn_{(IV)}$ aqueous solution is 80mM $SnCl_4 \cdot 5H_2O$ aqueous solution

and the optimum number of spinning is 5, with respect to photocurrent density.

In order to understand the cause of the enhanced photoelectric properties of the Fe_2O_3/$Fe_xSn_{1-x}O_4$/FeOOH photoanode compared with pristine hematite photoanode, a series of comparative

characterizations are carried out and interpreted below. The optical behavior of the samples is

evaluated by UV-visible spectroscopy. Diffuse reflectance UV-Vis spectra and corresponding Tauc-

Plots of samples are shown in **Figure 7**. The pristine Fe_2O_3 exhibits a characteristic absorption peak

near 600nm which agreed well with the band gap of 2.1 eV of Fe_2O_3. The absorption region of

Fe_2O_3/$Fe_xSn_{1-x}O_4$ and Fe_2O_3/$Fe_xSn_{1-x}O_4$/FeOOH samples is slightly wider, and absorption intensity is

a little stronger, as a result of the absorption of $Fe_xSn_{1-x}O_4$ and FeOOH layers. The bandgap obtained

from Tauc-Plots (inset) decreases a bit, which can be negligible. In general, there is not much difference

of the three samples in terms of photo-induced carriers.

The Mott–Schottky plots (see **Figure 8a**), which are collected from hematite photoanode at a frequency of 10 kHz, in dark, exhibit a nonlinear behavior. The positive slopes suggest that hematite is n-type semiconductor. The Mott–Schottky analysis is derived from a planar electrode model, and owing to the appeared nonlinear behavior, the flat band potentials could not be estimated. But the slopes, which suggest hematite is n-type semiconductor, could be used to estimate the electron donor densities (N_D).[20] The carrier densities for the bare hematite, Fe_2O_3/ $Fe_xSn_{1-x}O_4$, Fe_2O_3/FeOOH and Fe_2O_3/$Fe_xSn_{1-x}O_4$/FeOOH photoanodes are 2.31×10^{19} cm^{-3}, 7.80×10^{19} cm^{-3}, 2.63×10^{19} cm^{-3} and 9.30×10^{19} cm^{-3}. Clearly, FeOOH layer basically doesn't affect the carrier density, but $Fe_xSn_{1-x}O_4$ layer obviously increases carrier density of photoanode compared with that of pristine hematite photoanode.

To further prove that the charge injection efficiency of the photoanode is increased, 0.5 M H_2O_2 was added in electrolyte, for H_2O_2 is a well-known hole scavenger.[15c, 21]. The injection efficiency η_{surf} in **Figure 8b** is achieved through dividing J_{H_2O} photocurrent by $J_{H_2O_2}$ photocurrent.[22] It can be seen that, the charge injection efficiency of the Fe_2O_3/FeOOH photoanode is two times higher than that of the pristine hematite over the entire potential range. It proved that FeOOH is the efficient oxygen evolution catalyst. What's more, the η_{surf} value at 1.4 V$_{RHE}$ for the Fe_2O_3/$Fe_xSn_{1-x}O_4$/FeOOH photoanode increases by 25% compared with that of Fe_2O_3/FeOOH photoanode, which suggests that the $Fe_xSn_{1-x}O_4$ layer can greatly passivate surface defects and reduce the rate of electron-hole recombination.

To further explore the cause of the enhanced photoelectric properties, Nyquist plots of electrochemical impedance spectroscopy (EIS) are attained under AM 1.5G illumination (100

8

mW/cm^2), with a bias of 1.23 V *vs*. RHE (**Figure 8c, 8d**). **Figure 8d** is the drawing of partial

enlargement. The impedance spectra are fitted to an equivalent circuit, as shown, where R_s represents

all the series resistances of the PEC system, R_{trap} represents the resistance in the photoanode, $R_{ct,ss}$

represents the charge resistance across the photoanode/electrolyte interface, C_{bulk} represents the

capacitance in the depletion layer of the photoanode, and C_{ss} represents the capacitance at the surface

of the photoanode. The equivalent circuit parameters obtained from fitting EIS data are summarized

in **Table 1**. It can be seen that R_{trap} and $R_{ct,ss}$ of bare hematite photoanode are 94.94 Ω and 3825 Ω.

After coating FeOOH layer, $R_{ct,ss}$ decreases to 2335 Ω, but R_{trap} changes from 94.94 Ω to 191.2 Ω. It

indicates that there are much defects existing in the interface between hematite and FeOOH layer.

Subsequently, after overlying Fe$_x$Sn$_{1-x}$O$_4$ layer between them, values of R_{trap} and $R_{ct,ss}$ have reached

the optimum, 61.53 Ω and 1045 Ω, respectively. This result indicates that Fe$_x$Sn$_{1-x}$O$_4$ layer not only

decreases the resistance of electrode interior, but also reduces the resistance across the

photoanode/electrolyte interface. The decreased resistance of photoanode interior can improve the

charge separation, which is the major contributing factor for the pronounced photocurrent

improvement in Fe$_2$O$_3$/Fe$_x$Sn$_{1-x}$O$_4$/FeOOH photoanode compared with that of Fe$_2$O$_3$/FeOOH

photoanode.

3. **Conclusion**

In summary, a very facile method is used to fabricate Fe$_2$O$_3$/Fe$_x$Sn$_{1-x}$O$_4$/FeOOH photoanode and

Fe$_x$Sn$_{1-x}$O$_4$ passivation layer and FeOOH catalyst are investigated in detail. The photocurrent densities

improved by 66.2% and 84.4% at 1.23 V *vs*. RHE, with passivation layer and catalytic layer,

respectively, compared with that of bare Fe$_2$O$_3$. What's more, the photocurrent densities of

$Fe_2O_3/Fe_xSn_{1-x}O_4/FeOOH$ photoanode improved by 121.1% at 1.23 V *vs*. RHE. The primary reason for the increase of photocurrent density is that not only the $Fe_xSn_{1-x}O_4$ layer greatly passivates surface defects and reduce the rate of electron-hole recombination, but also catalytic layer improves reaction kinetics. Furthermore, the $Fe_xSn_{1-x}O_4$ interlayer simultaneously decreases the resistance of electrode interior and the resistance across the electrode/electrolyte interface. The method used to fabricate $Fe_xSn_{1-x}O_4$ interlayer is extremely easy, which can be widely applied to overlie various interlayers between semiconductor electrode and catalytic layer.

4.   **Experimental section**

4.1 **Synthesis of Fe₂O₃ photoanode:** The highly disordered wormlike Fe_2O_3 films were prepared by pyrolysis of appropriate amount ferrocene in a crucible,[4c] which covered by a fluorine-doped SnO_2 glass (FTO, Nippon Sheet Glass, Japan, 14 ohm sq^{-1}). The optimum amount of ferrocene is 100 mg and the optimum pyrolysis temperature is 500 ℃, with respect to photocurrent density. Before PEC measurements, the photoanode was annealed at 750 °C for 10 min.

Synthesis of Fe₂O₃/FeₓSn₁₋ₓO₄ photoanode: To deposit $Fe_xSn_{1-x}O_4$ onto Fe_2O_3 surface, a simple spin-coated method was applied. The $Fe_xSn_{1-x}O_4$ layer was prepared by spin-coating Sn (IV) aqueous solution on the above film. The $SnCl_4$ $5H_2O$ (Sigma-Aldrich, 98 %) aqueous solution (pH=1) was freshly prepared and spin-coated on the above film several times. And then the substrates were heated at 100 °C for 10 min. A series of $SnCl_4$ $5H_2O$ aqueous solution was studied, including 20, 40, 80, 120 and 180 mM. And several spin-coating times were attempted. No need to treat with NaOH aqueous solution, which may induce a lot surface defects. Before measurements, the photoanode was annealed at 750 °C for 10 min.

Synthesis of multicomponent Fe₂O₃/FeₓSn₁₋ₓO₄/FeOOH photoanode: The FeOOH catalytic layer was coated on $Fe_2O_3/Fe_xSn_{1-x}O_4$ photoanode by chemical bath deposition method. The layer was formed by immersing electrode into an aqueous solution of $FeCl_3$ 6 H_2O (0.025 M) and $NaNO_3$ (1 M) at 100 ℃ for 10 min after annealed at 750 ℃ for 10 min. The substrates were thoroughly rinsed in DI water to remove any residue ions and surface precipitation. And then the substrates were heated at 200 ℃ for 3 hours.

4.2 **Characterization.** The morphology and nanostructure of the samples were characterized by field emission scanning electron microscopy (FESEM, FEI QUANTA 3D FESEM, 5kV) and transmission electron microscopy (TEM, FEI Tecnai F30 S-TWIN). X-ray diffraction (XRD) patterns were obtained on a Rigaku DMAX-RB using Cu Kα X-ray radiation source to determine the crystal phase of the obtained samples. X-Ray photoelectron spectra were recorded on a Kratos AXIS Ultra DLD with a monochromatic Al Kα source (1486.6 eV). The UV-Visible absorption spectra were recorded on a UV–vis-NIR spectrophotometer (Varian Cary 5000).

4.3 **PEC measurements.** All PEC measurements were carried out using CHI 660D electrochemical workstation in a three-electrode electrochemical cell with a Pt wire as a counter electrode and an Ag/AgCl electrode as a reference. The as-prepared hematite samples were made into working electrodes, with a working area of 0.2 cm^2. The electrolyte was an aqueous solution of NaOH with a pH of 13.6, bubbled with N_2 for 20 min before measurement. The irradiation source was provided by a solar simulator (Oriel, 94023A), with a light intensity of about 100 mW/cm^2 estimated with a radiometer. In a typical experiment, the potential was swept from 0.4 V to 1.7 V *vs*. RHE at a scan rate of 50 mV/s. Capacitance was derived from the electrochemical impedance obtained at

11

each potential with 10000 Hz frequency in the dark. Mott–Schottky plots were generated from the

capacitance values. Electrochemical impedance spectroscopy (EIS) measurement was carried out

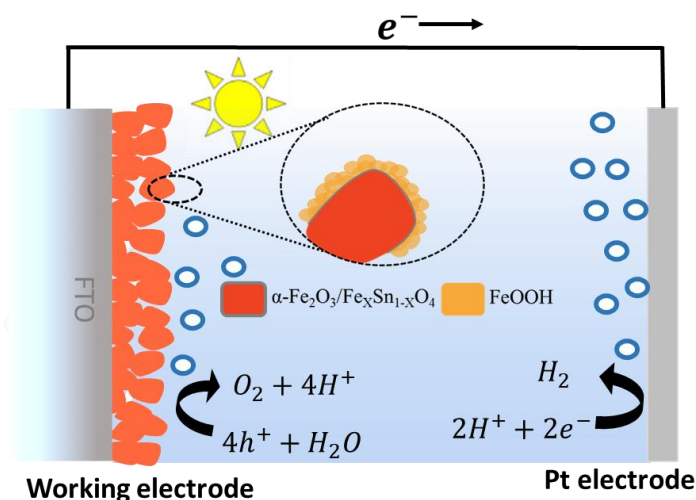in the same workstation with a frequency range of 0.1–100 kHz at the potential of 1.23 V *vs*. RHE.

Figure 1. Cross-sectional schematic of the designed multicomponent $Fe_2O_3/Fe_xSn_{1-x}O_4/FeOOH$ photoanode for water oxidation.
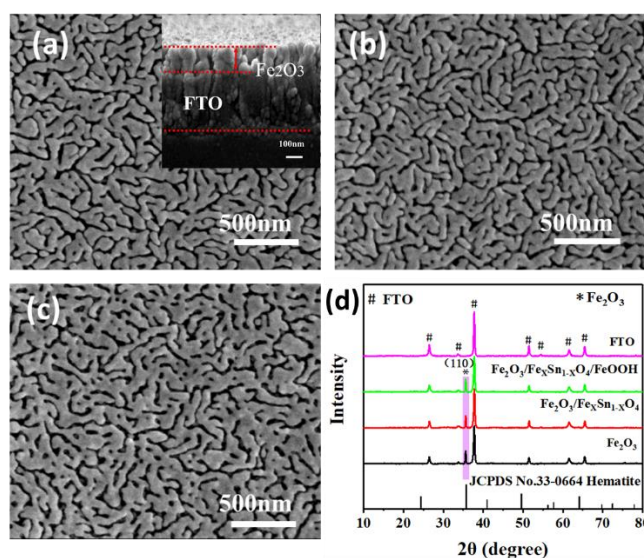
Figure 2. SEM images for the (a) bare Fe_2O_3 (inset: cross-section image); (b) $Fe_2O_3/Fe_xSn_{1-x}O_4$; (c) $Fe_2O_3/Fe_xSn_{1-x}O_4/FeOOH$ photoanodes. (d) X-ray diffraction patterns for the FTO, bare Fe_2O_3, $Fe_2O_3/Fe_xSn_{1-x}O_4$ and $Fe_2O_3/Fe_xSn_{1-x}O_4/FeOOH$ thin films.
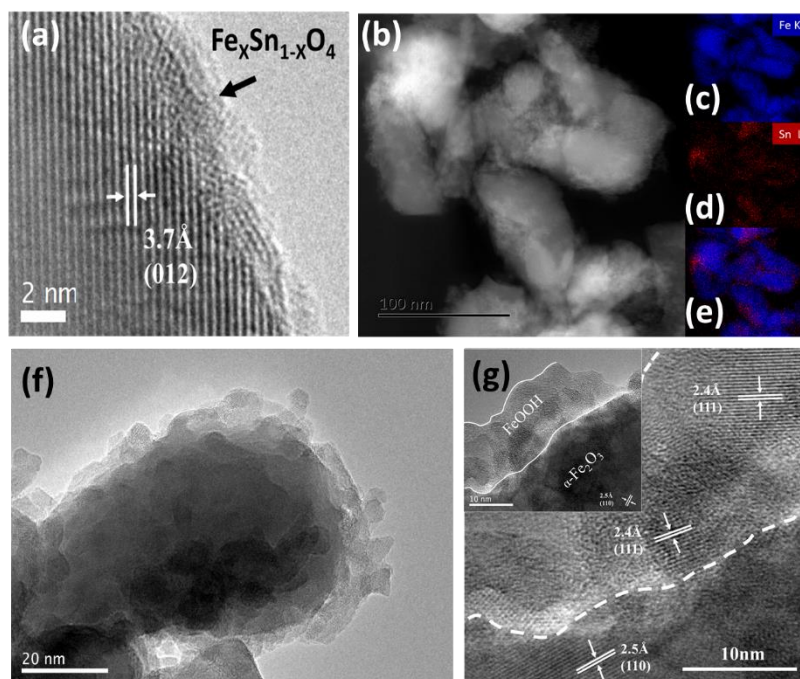
Figure 3. (a) HRTEM image of $Fe_2O_3/Fe_xSn_{1-x}O_4$ photoanode. (b) STEM image of $Fe_2O_3/Fe_xSn_{1-x}O_4/FeOOH$ nanoparticles; (c)–(e) Maps for elemental Fe, Sn and Fe/Sn. (f) HRTEM image of hematite decorated with FeOOH nanosheets. (g) HRTEM images of $Fe_2O_3/Fe_xSn_{1-x}O_4/FeOOH$ thinfilm.
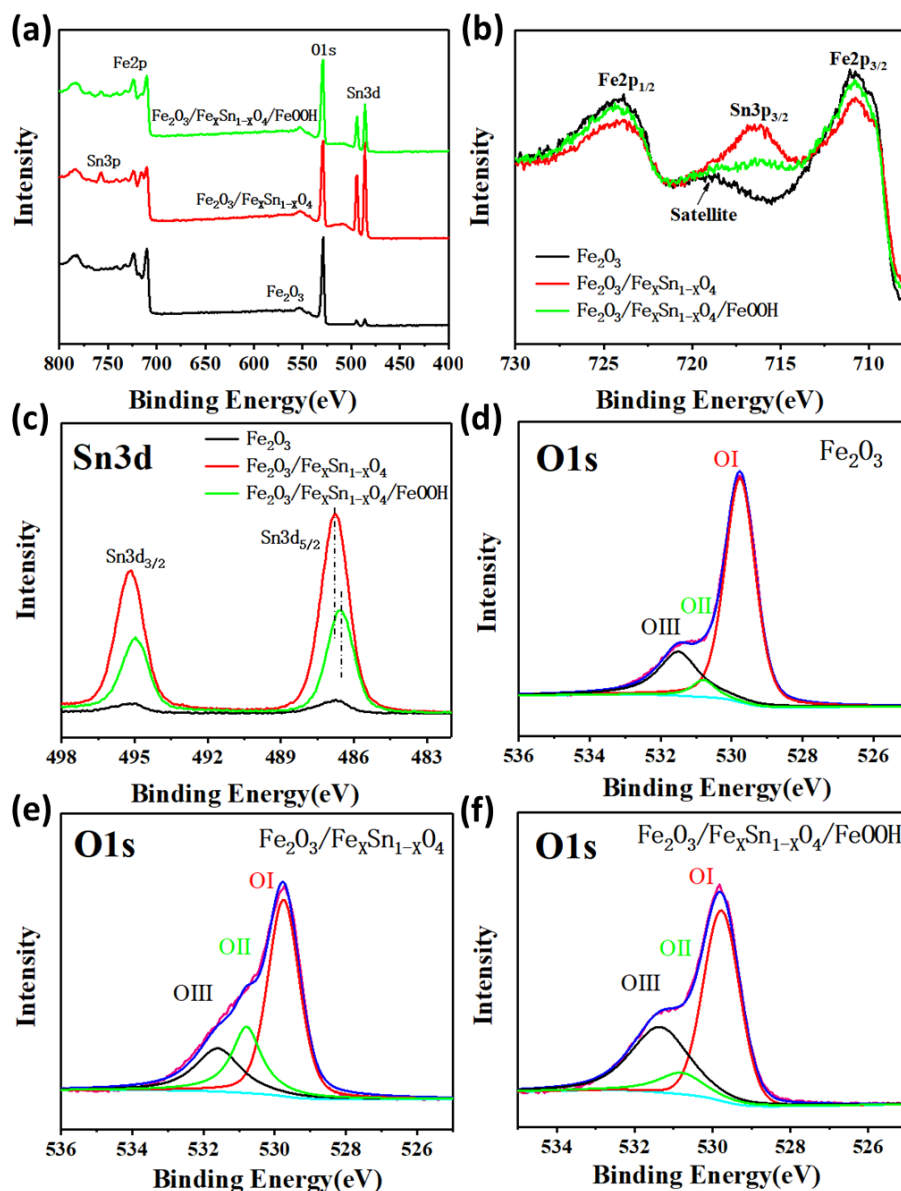
Figure 4. XPS spectra of (a) survey, (b) Fe 2p, (c) Sn 3d, (d)-(f) O 1s for the bare Fe_2O_3, $Fe_2O_3/Fe_xSn_{1-x}O_4$, and $Fe_2O_3/Fe_xSn_{1-x}O_4/FeOOH$ thin films.
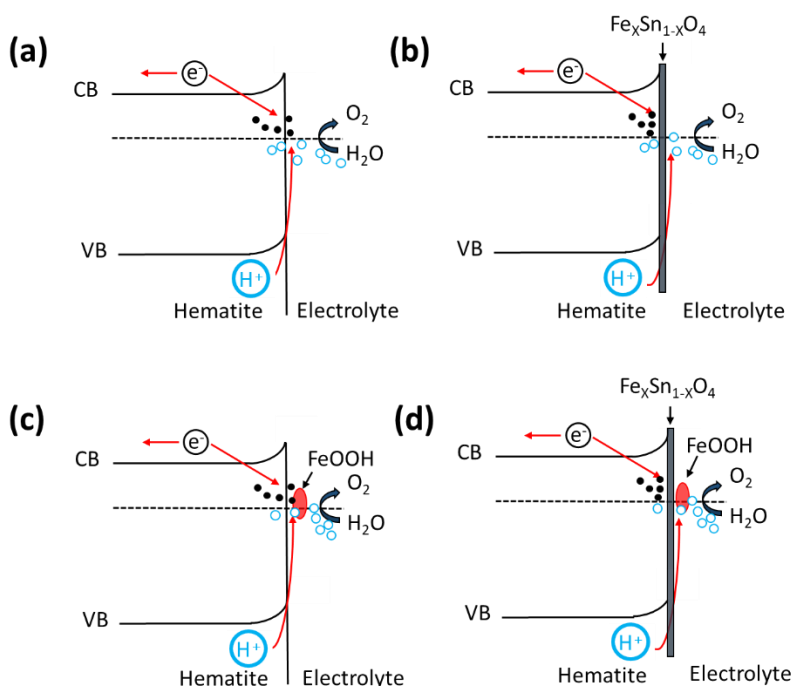
Figure 5. (a) Surface defect states in the band structure; (b) Application of a thin noncatalytic surface layer to passivate defect states; (c) Application of an OER catalyst layer; (d) The synergetic benefits of passivation layer and catalytic layer for efficient water splitting
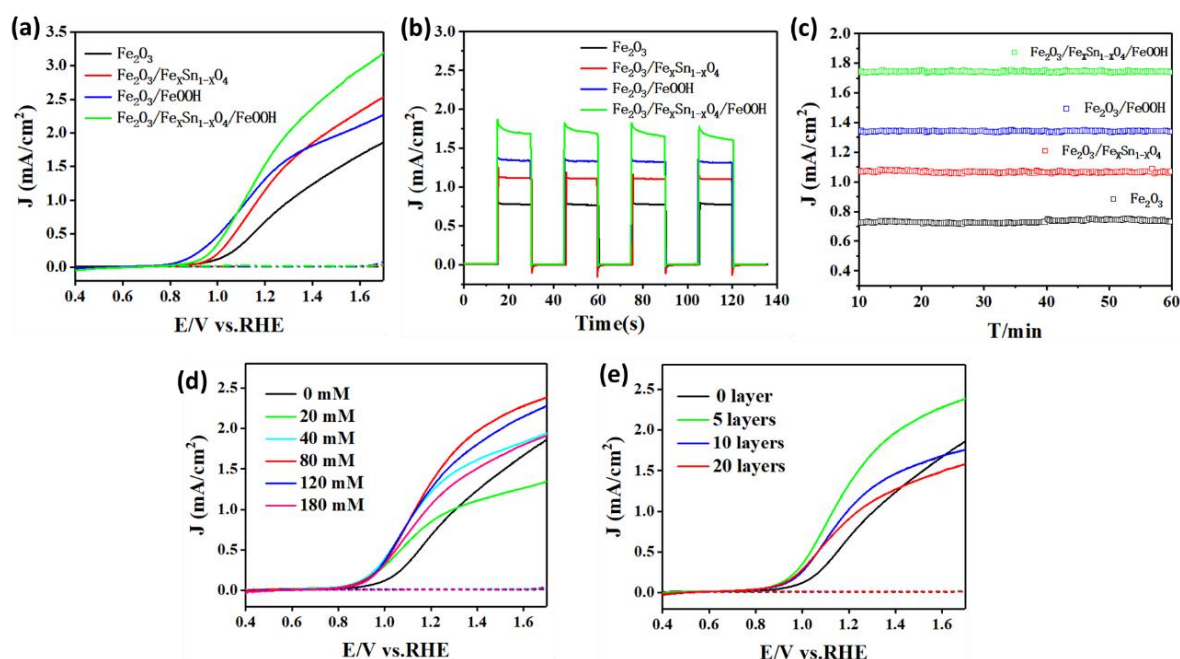

Figure 6. (a) J–V characteristics of bare Fe_2O_3, $Fe_2O_3/Fe_xSn_{1-x}O_4$, $Fe_2O_3/FeOOH$ and $Fe_2O_3/Fe_xSn_{1-x}O_4/FeOOH$ photoanodes in dark and light illumination (100 mW/cm^2). (b) Short-circuit photocurrent response of bare Fe_2O_3, $Fe_2O_3/Fe_xSn_{1-x}O_4$, $Fe_2O_3/FeOOH$ and $Fe_2O_3/Fe_xSn_{1-x}O_4/FeOOH$ photoanodes at 1.23V *vs*. RHE. (c) Photochemical stability curves of bare Fe_2O_3, $Fe_2O_3/Fe_xSn_{1-x}O_4$, $Fe_2O_3/FeOOH$ and $Fe_2O_3/Fe_xSn_{1-x}O_4/FeOOH$ photoanodes collected at 1.23V *vs*. RHE. (d), (e) J–V characteristics of $Fe_2O_3/Fe_xSn_{1-x}O_4$ photoanode with different preparation parameters in dark and light illumination.
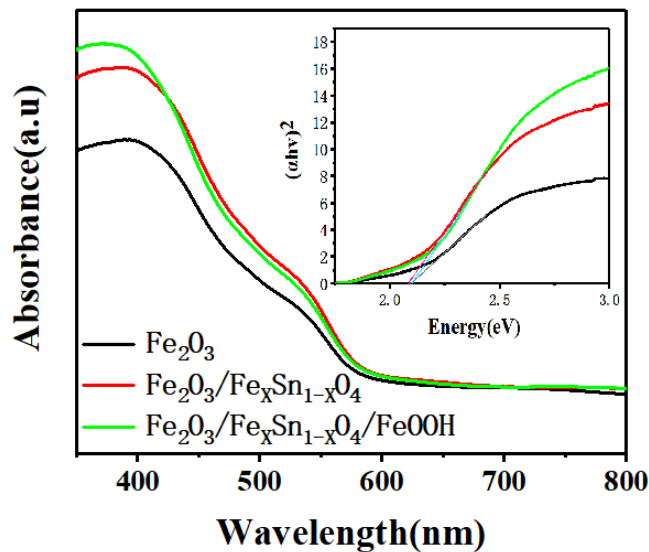
15

Figure 7. UV-VIS diffuse reflectance for the bare Fe_2O_3, $Fe_2O_3/Fe_xSn_{1-x}O_4$ and $Fe_2O_3/Fe_xSn_{1-x}O_4$/FeOOH thin films, the inset shows the Tauc-Plots.
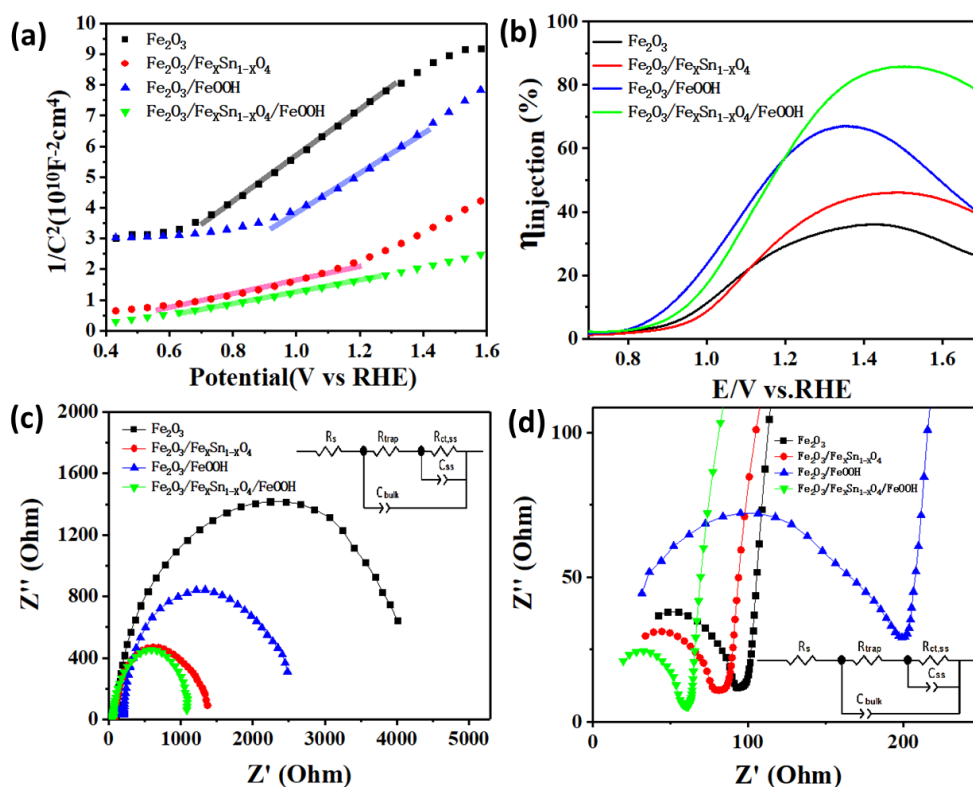
Figure 8. (a) Mott-Schottky plots of the bare Fe_2O_3, $Fe_2O_3/Fe_xSn_{1-x}O_4$, $Fe_2O_3/FeOOH$ and $Fe_2O_3/Fe_xSn_{1-x}O_4/FeOOH$ thin films, the inset shows the Tauc-Plots. (b) Injection yields of bare Fe_2O_3, $Fe_2O_3/Fe_xSn_{1-x}O_4$, $Fe_2O_3/FeOOH$ and $Fe_2O_3/Fe_xSn_{1-x}O_4/FeOOH$ photoanodes under illumination of 100 mW/cm². (c), (d) EIS Nyquist plots of bare Fe_2O_3, $Fe_2O_3/Fe_xSn_{1-x}O_4$, $Fe_2O_3/FeOOH$ and $Fe_2O_3/Fe_xSn_{1-x}O_4/FeOOH$ photoanodes under illumination of 100 mW/cm².

Table 1

16

Carrier densities and resistance values of bare Fe_2O_3, $Fe_2O_3/Fe_xSn_{1-x}O_4$, $Fe_2O_3/FeOOH$ and $Fe_2O_3/Fe_xSn_{1-x}O_4/FeOOH$ photoanodes.

Photoanodes	Mott-Schottky Curves	Nyquist Curves	
	$N_D/10^{19}cm^{-3}$	R_{trap}/Ω	$R_{ct,ss}/\Omega$
Fe_2O_3	2.31	94.94	3825
$Fe_2O_3/Fe_xSn_{1-x}O_4$	7.80	84.6	1236
$Fe_2O_3/FeOOH$	2.63	191.2	2335
$Fe_2O_3/Fe_xSn_{1-x}O_4/FeOOH$	9.30	61.53	1045

Corresponding Authors

Yan, E-mail: xqyan@mater.ustb.edu.cn

Z. Bai, E-mail: baizhiming2008@126.com

Acknowledgment

References

[1]   a) Z. Luo, C. Li, S. Liu, T. Wang, J. Gong, *Chem Sci* **2017**, 8, 91; b) S. Cao, X. Yan, Z. Kang, Q. Liang, X. Liao, Y. Zhang, *Nano Energy* **2016**, 24, 25; c) S. J. A. Moniz, S. A. Shevlin, D. J. Martin, Z.-X. Guo, J. Tang, *Energy & Environmental Science* **2015**, 8, 731; d) A. G. Tamirat, J. Rick, A. A. Dubale, W.-N. Su, B.-J. Hwang, *Nanoscale Horizons* **2016**, 1, 243; e) Z. Bai, X. Yan, Z. Kang, Y. Hu, X. Zhang, Y. Zhang, *Nano Energy* **2015**, 14, 392.

[2]   a) Y. W. Phuan, W.-J. Ong, M. N. Chong, J. D. Ocon, *Journal of Photochemistry and Photobiology C: Photochemistry Reviews* **2017**, 33, 54; b) P. Luan, M. Xie, X. Fu, Y. Qu, X. Sun, L. Jing, *Physical chemistry chemical physics : PCCP* **2015**, 17, 5043.

[3]   J. Su, J. Wang, C. Liu, B. Feng, Y. Chen, L. Guo, *RSC Advances* **2016**, 6, 101745.

[4]   a) L. Xi, S. Y. Chiam, W. F. Mak, P. D. Tran, J. Barber, S. C. J. Loo, L. H. Wong, *Chem. Sci.* **2013**, 4, 164; b) D. Cao, W. Luo, J. Feng, X. Zhao, Z. Li, Z. Zou, *Energy Environ. Sci.* **2014**, 7, 752; c) J. Deng, X. Lv, J. Gao, A. Pu, M. Li, X. Sun, J. Zhong, *Energy & Environmental Science* **2013**, 6, 1965.

[5]   a) M. Rioult, H. Magnan, D. Stanescu, A. Barbier, *The Journal of Physical Chemistry C* **2014**, 118, 3007; b) G. K. Mor, H. E. Prakasam, O. K. Varghese, K. Shankar, C. A. Grimes, *Nano letters* **2007**, 7, 2356.

[6]   a) Y. Ling, Y. Li, *Particle & Particle Systems Characterization* **2014**, 31, 1113; b) K. D. Malviya, D. Klotz, H. Dotan, D. Shlenkevich, A. Tsyganok, H. Mor, A. Rothschild, *The Journal of Physical Chemistry C* **2017**, 121, 4206; c) Z. Xu, H.

17

Wang, Y. Wen, W. Li, C. Sun, Y. He, Z. Shi, L. Pei, Y. Chen, S. Yan, *ACS applied materials & interfaces* **2018**, 10, 3624; d) Z. Xu, S. C. Yan, Z. Shi, Y. F. Yao, P. Zhou, H. Y. Wang, Z. G. Zou, *ACS applied materials & interfaces* **2016**, 8, 12887.

[7]   a) C. R. Cox, M. T. Winkler, J. J. H. Pijpers, T. Buonassisi, D. G. Nocera, *Energy Environ. Sci.* **2013**, 6, 532; b) J. Y. Kim, D. H. Youn, K. Kang, J. S. Lee, *Angewandte Chemie* **2016**, 55, 10854.

[8]   a) J. Y. Kim, J.-W. Jang, D. H. Youn, G. Magesh, J. S. Lee, *Advanced Energy Materials* **2014**, 4, 1400476; b) M. G. Ahmed, I. E. Kretschmer, T. A. Kandiel, A. Y. Ahmed, F. A. Rashwan, D. W. Bahnemann, *ACS applied materials & interfaces* **2015**, 7, 24053.

[9]   F. Le Formal, N. Tétreault, M. Cornuz, T. Moehl, M. Grätzel, K. Sivula, *Chem. Sci.* **2011**, 2, 737.

[10]   B. Klahr, S. Gimenez, F. Fabregat-Santiago, J. Bisquert, T. W. Hamann, *Journal of the American Chemical Society* **2012**, 134, 16693.

[11]   Q. Yu, X. Meng, T. Wang, P. Li, J. Ye, *Advanced Functional Materials* **2015**, 25, 2686.

[12]   a) K. J. McDonald, K.-S. Choi, *Chemistry of Materials* **2011**, 23, 4863; b) R. L. Spray, K. J. McDonald, K.-S. Choi, *The Journal of Physical Chemistry C* **2011**, 115, 3497.

[13]   a) J. Y. Kim, G. Magesh, D. H. Youn, J. W. Jang, J. Kubota, K. Domen, J. S. Lee, *Scientific reports* **2013**, 3, 2681; b) M. Cornuz, M. Grätzel, K. Sivula, *Chemical Vapor Deposition* **2010**, 16, 291.

[14]   W. D. Chemelewski, H. C. Lee, J. F. Lin, A. J. Bard, C. B. Mullins, *Journal of the American Chemical Society* **2014**, 136, 2843.

[15]   a) S. Sultana, S. Mansingh, K. M. Parida, *Journal of Materials Chemistry A* **2018**, 6, 11377; b) G. Wang, Y. Ling, D. A. Wheeler, K. E. George, K. Horsley, C. Heske, J. Z. Zhang, Y. Li, *Nano letters* **2011**, 11, 3503; c) T. Hisatomi, H. Dotan, M. Stefik, K. Sivula, A. Rothschild, M. Gratzel, N. Mathews, *Advanced materials* **2012**, 24, 2699; d) A. Kleimanshwarsctein, Y. S. Hu, A. J. Forman, G. D. Stucky, E. W. Mcfarland, *Journal of Physical Chemistry C* **2008**, 112, 15900.

[16]   A. Bak, W. Choi, H. Park, *Applied Catalysis B: Environmental* **2011**, 110, 207.

[17]   J. Wang, W. Cui, Q. Liu, Z. Xing, A. M. Asiri, X. Sun, *Advanced materials* **2016**, 28, 215.

[18]   a) I. D. Welsh, P. M. A. Sherwood, *Physical Review B* **1989**, 40, 6386; b) N. S. Mcintyre, D. G. Zetaruk, *Analytical Chemistry* **1977**, 49, 1521.

[19]   M. Kwoka, L. Ottaviano, M. Passacantando, S. Santucci, G. Czempik, J. Szuber, *Thin Solid Films* **2005**, 490, 36.

[20]   F. Cardon, W. P. Gomes, *Journal of Physics D* **1978**, 11.

[21]   a) H. Dotan, K. Sivula, M. Grätzel, A. Rothschild, S. C. Warren, *Energy Environ. Sci.* **2011**, 4, 958; b) O. Zandi, T. W. Hamann, *The Journal of Physical Chemistry Letters* **2014**, 5, 1522.

[22]   L. Gao, F. Li, H. Hu, X. Long, N. Xu, Y. Hu, S. Wei, C. Wang, J. Ma, J. Jin, *ChemSusChem* **2018**.

Abstract Graphic